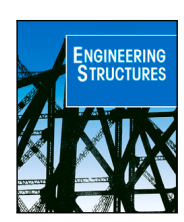
ELSEVIER

Contents lists available at ScienceDirect

# **Engineering Structures**

journal homepage: www.elsevier.com/locate/engstruct





# Plastic hinge length in reinforced HPFRCC beams and columns

Joseph A. Almeida, Matthew J. Bandelt \*

John A. Reif, Jr., Department of Civil and Environmental Engineering, New Jersey Institute of Technology, 323 Dr. Martin Luther King Jr. Blvd, Newark, 07102, NJ, USA

#### ARTICLE INFO

Keywords:
Plastic hinge length
Rotation capacity
HPFRCC
UHPC
ECC
Axial load
Column
Beam

#### ABSTRACT

The use of ductile concrete materials such as High Performance Fiber Reinforced Cementitious Composites (HPFRCCs) within plastic hinge regions of structural components has garnered research interest in order to improve the seismic resistance of reinforced concrete structures. While experimental and numerical results appear promising in reducing component damage and probability of system level collapse, accurate nonlinear analysis tools capable of capturing the influence of axial load well into a component's inelastic regime is needed. In this study, a series of 180 high fidelity numerical simulations of HPFRCC beam—column elements are simulated and used to calibrate new plastic hinge length expressions for concentrated and distributed plasticity models for use in system level structural analysis. The numerical models cover a range of HPFRCC material properties, reinforcement ratios, shear span lengths, and axial load levels. The ability of the newly developed expressions to predict component inelastic rotations are subsequently compared to hinge length expressions in the literature and the inelastic rotations of 47 experimental components. The results of this study provide new insights into the effects of axial load on the plastic hinge behavior of HPFRCC components, significantly improves on the accuracy of past plastic hinge length expressions allowing for more accurate modeling of HPFRCC component responses and system level behavior.

# 1. Introduction

The development of performance based seismic design (PBSD) has widely been regarded as the next step in creating resilient communities [1]. By explicitly quantifying and comparing structural responses against discrete levels of performance, key stakeholder metrics such as the potential economic losses and time to recovery can be estimated and weighted [1]. Thus, controlling and quantifying the levels of structural damage is fundamental to PBSD and the impact on a community's resilience.

Over the past three decades, highly ductile concrete materials termed high-performance fiber reinforced cementitious composites (HPFRCCs) have been developed to exhibit enhanced mechanical performance and durability [2] in comparison to traditional concrete. The material level performance of HPFRCCs is largely derived from the addition of small discontinuous fibers and mixture optimization [3] resulting in a multiple micro-cracking behavior in tension [4,5]. When reinforced with longitudinal steel, HPFRCC components have been shown to improve ductility, increase strength, lower stiffness degradation, and significantly enhance damage tolerance in comparison to reinforced concrete components [6–10]. Therefore, recent research

endeavors have focused on the seismic application of HPFRCC materials in structural systems in order to improve the seismic response of structures [8,11–14].

The ever-growing adoption of PBSD and the increasing merits of HPFRCC use to improve structural performance necessitates accurate modeling tools in order to evaluate and compare the system-level behavior of reinforced HPFRCC structures. To this end, in a series of studies by Genturk and Elnashai [11] and Tariq et al. [13], component models based on distributed and concentrated plasticity methods were developed and validated against experimental force-drift responses. The component model developed by Genturk and Elnashai [11] was subsequently used to evaluate the life-cycle cost between reinforced concrete, HPFRCC, and mixed material structures subjected to ground motions [15]. It was demonstrated through appropriate optimization and design that reinforced concrete structures employing HPFRCCs within their plastic hinge regions offer a 17% lower life-cycle cost and an 18% increase in base shear capacity. The advantages of deploying HPFRCC materials within reinforced concrete systems were further underlined by Tariq et al. [13]. Structures using HPFRCC materials in high damage zones were reported to have a 38% lower probability

E-mail addresses: ja558@njit.edu (J.A. Almeida), bandelt@njit.edu (M.J. Bandelt).

Corresponding author.

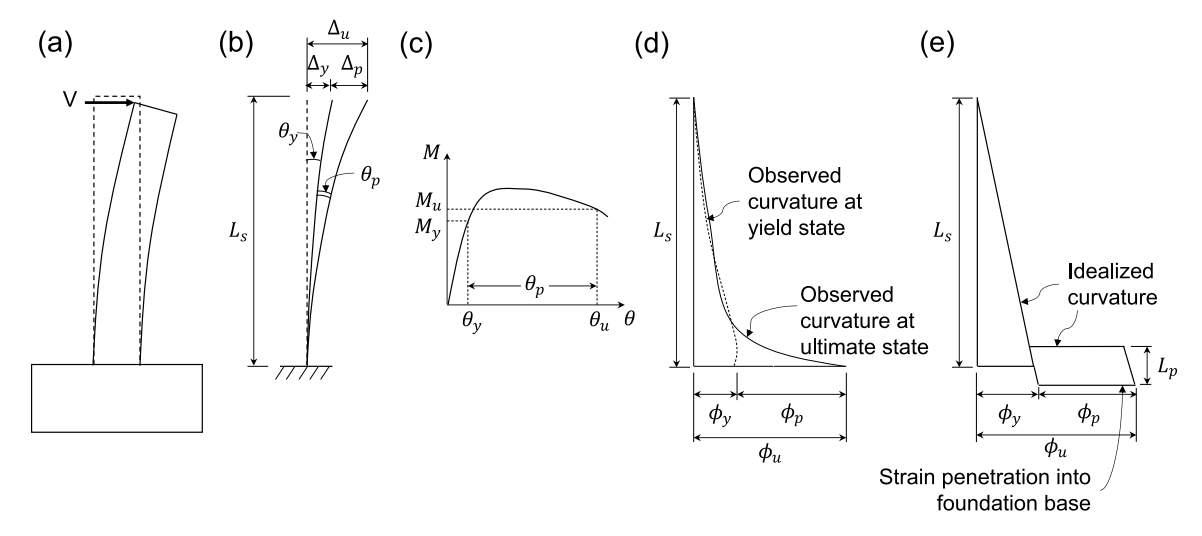


Fig. 1. Theoretical approach of equivalent plastic hinge length (a) cantilever column with lateral load, (b) idealized cantilever column, (c) component moment rotation response, (d) actual curvature distribution, and (e) idealized curvature distribution.

of collapse under a maximum considered earthquake than fully reinforced concrete structures with the caveat that the unique mechanical behavior of HPFRCC materials is considered in the design of structural elements

However, several shortcomings exist in the previously developed component models used in the aforementioned studies. Namely, the distributed plasticity model used by Genturk and Elnashai [11] has comparatively higher computational costs associated with the nonlinear fiber sections modeled across the full span of the components rather than over a finite length. In contrast, Tariq et al. [13] used computationally efficient spring-hinge models that accounted for reinforcement fracture, which is the dominant failure mechanism of reinforced HPFRCC flexural elements [16,17]. The plastic hinge length expressions used to derive the monotonic backbone curves did not, however, consider the deteriorating effects of axial load [18]. When modeling the near collapse regime of structures, inelastic plastic hinge regions can inevitably form within columns and result in lower lateral deformation capacities at the component [19,20] and system level [21]. To further facilitate the use of HPFRCCs for seismic applications, improved plastic hinge models must be developed for engineers and researchers that can be used to assess system-level performance in a range of components where HPFRCC materials may be used. Therefore, this study aims to (1) quantify the effects of axial load on plastic hinge length through a previously validated numerical framework, (2) develop a set of new monotonic plastic hinge length expressions for beam-columns that are capable of accurately predicting experimental component rotation capacities and (3) evaluate the relative performance prediction capabilities of plastic hinge length expressions in regards to element rotational capacities.

# 2. Background

#### 2.1. Equivalent plastic hinge length formulation

The estimation of a component's lateral deformation capacity is realized through the connection of section curvature and member chord rotation [22]. As illustrated in Fig. 1a and b, a column sub-assemblage subjected to a lateral load is idealized as a fixed cantilever column of a shear span length,  $L_s$ .

As the column is laterally loaded, the corresponding bending moment and chord rotation is tracked (see Fig. 1c) where  $\theta_y$  ( $\Delta_y/L_s$ ) and  $\theta_u$  ( $\Delta_u/L_s$ ) denote the yield and ultimate rotation of the component, respectively. Thus, by integrating the section curvature along the column

span in Fig. 1d, the ultimate rotation of the column can be determined as:

$$\theta_u = \int_0^{L_s} \phi_u(z) dz \tag{1}$$

Further observation of Fig. 1c shows that the ultimate rotational capacity can be established as a summation of the yield and plastic rotations. By applying the same curvature integration approach of Eq. (1), the ultimate rotation is redefined as:

$$\theta_u = \theta_y + \theta_p = \int_0^{L_s} \phi_y(z) dz + \int_0^{L_s} [\phi_u(z) - \phi_y(z)] dz$$
 (2)

While Eqs. (1) and (2) present the theoretical connection between section curvature and member chord rotation, the nonlinear curvature distribution shown in Fig. 1d is rarely known, thus, simplifying approximations can be made (see Fig. 1e) such that:

$$\theta_u \approx \frac{1}{2}\phi_y L_s + (\phi_u - \phi_y) L_p \tag{3}$$

where  $\phi_y$  and  $\phi_u$  are the section curvatures determined by section analysis at the yield and ultimate displaced states, respectively, and  $L_p$ , is the equivalent plastic hinge length – often termed plastic hinge length – over which plastic curvature is assumed to be constant. By rearranging Eq. (3), the equivalent plastic hinge length can be expressed as:

$$L_p = \frac{\theta_u - \theta_y}{\phi_u - \phi_y} \tag{4}$$

Thus far in this discussion, the formulation connecting section curvatures and a component's rotation capacity has been based on the assumptions of the Euler–Bernoulli theorem, and as a result, the calculated rotation capacity has considered flexural deformations only. Discrepancies arise when comparing the theoretical and actual component rotations due to the addition of shear and fixed-end deformations from bond slip and strain penetration. To resolve the discrepancies, plastic hinge length expressions used to predict  $L_p$  of Eq. (4) utilize actual component rotations and curvatures. In the context of this study,  $\theta_y$ ,  $\theta_u$ ,  $\phi_y$ , and  $\phi_u$  are numerically calculated using high fidelity models where:

$$\phi_i = \frac{\varepsilon_{ts}}{d - c} \tag{5}$$

d is the effective depth, c is the depth to the neutral axis, and  $\varepsilon_{ts}$  is the strain in the extreme layer of tension reinforcement at the yield (for  $\phi_y$ ) or ultimate component rotation (for  $\phi_u$ ). The yield and ultimate

**Table 1**Select plastic hinge length expressions.

Reference	Expressions	Component	Material	Loading
Pauley and Priestly [22]	$\beta_0 L_s + \beta_1 d_b f_y$	Beam & Column	Concrete	Cyclic
Panagiotakos and Fardis [19]	$\beta_0 L_s + \beta_1 \alpha_{sl} d_b f_v$	Beam & Column	Concrete	Mono. & Cylic
Bae and Bayrak [23]	$[\beta_0(P/P_0) + \beta_1(A_s/A_g) - \beta_2]L_s + \beta_3 h$	Beam & Column	Concrete	Cyclic
Wang et al. [24]	$\beta_0 L_s + d_b f_v / \beta_1 \sqrt{f_c'}$	Segmental Column	HPFRCC	Cyclic
Tariq et al. [12]	$(\beta_0 + \beta_1 \rho)d$	Beam	HPFRCC	Cyclic
Pokhrel and Bandelt [18]	$\beta_0 L_s + \beta_1 \rho f_y / f_t$	Beam	HPFRCC	Mono. & Cyclic

Selected plastic hinge length expressions reported in the literature for reinforced concrete and HPFRCC components. Regression coefficients,  $\beta$ , vary based on boundary conditions, loading protocol, and experimental values used for calibration.

rotations are determined using the following criteria, respectively: (1) the tension reinforcement reaches its yield strain, and (2) the tension reinforcement reaches an ultimate strain of 18% or the lateral load carrying capacity decreases by 20%. It is additionally noted that the tension reinforcement strain was used to calculate the ultimate component rotation because reinforced HPFRCC component failure modes are predominantly governed by reinforcement fracture [16,17].

# 2.2. Previous plastic hinge length expressions

In resolving the discrepancies between theoretically calculated and experimentally observed component rotations in Section 2.1, the calculated plastic hinge length was required to account for flexure, shear, and fixed-end rotations. As a result, several variables influencing the deformation of components have been proposed in plastic hinge length expressions resulting in considerable variability amongst studies as shown in Table 1. The primary variables often considered include shear span length,  $L_s$ , column section height, h, and column effective depth, d, as governing factors of flexure and shear [18,19,22–24]. Variables such as reinforcement bar diameter,  $d_b$ , tensile yield strength,  $f_y$ , and the concrete compressive strength,  $\sqrt{f_c}$ , have been proposed as governing factors of bond–slip and strain penetration [18,19,22,24]. In addition, the effects of loading protocol (i.e., monotonic versus cyclic loading) are also typically quantified, but implicit in coefficients within plastic hinge length expressions [18,19].

The effects of axial load level on plastic hinge length have been particularly subject to debate for some time despite known axial–flexure–shear interactions in structural components [25–27]. In a number of earlier studies for reinforced concrete [28,29], plastic hinge length was reported to be insensitive to axial load level. In contrast, research by Bae et al. [23] concluded that plastic hinge length is insensitive to axial load levels,  $P/A_g f_c'$ , under 20% but linearly increased with axial load ratios above 20%. Interestingly, in the work of Panagiotakos and Fardis [19], the proposed rotation expressions explicitly account for the axial load level, while their plastic hinge length expressions do not. Thus, it is not inherently clear whether a component's plastic hinge length is a function of axial load or whether it can simply be accounted for in the calculated section curvatures.

In the context of reinforced HPFRCC components, several plastic hinge length expressions have been developed and have largely been limited to flexural beams [12,18,24]. Among these studies, work by Pokhrel and Bandelt [18] systematically identified the effects of material properties, boundary conditions, loading scheme, and component geometry through numerical modeling that was then verified against physical experiments. Pokhrel and Bandelt [18] concluded that similar to reinforced concrete expressions, increases in shear span length and, therefore, changes in moment gradient and shear demand resulted in increases in the plastic hinge length. However, due to the unique tension stiffening behavior of reinforced HPFRCCs and its effects on the spread of plasticity, an additional term of the ratio of relative tensile strengths,  $\rho f_y/f_t$ , between the tension reinforcement and HPFRCC tensile strength was proposed. The relative performance of both expressions was shown to be a significant improvement over prior studies,

with an average prediction accuracy within 15% of experimental values in contrast to the 40%–239% overprediction of other expressions presented in the literature. However, the work by Pokhrel and Bandelt [18] exclusively considered members without axial load, and, as previously discussed, efforts must be made to elucidate axial load effects.

## 3. Numerical experiments

Recent advancements in HPFRCC constitutive material models have resulted in numerical simulation tools that are capable of capturing the flexural response of structural elements into the collapse level regime [30-33]. This numerical framework has enabled researchers to systematically investigate the effects of design parameters on flexural response [17,18,31]. Building on these research approaches, the numerical framework is extended to the investigation of 180 reinforced HPFRCC beam-column elements subjected to combined axial loading and bending across a range of design and loading parameters using a commercially available finite element program, DIANA FEA 10.5 [34]. Five different HPFRCC material mixtures including Hybrid Fiber Reinforced Concrete (HyFRC), Engineered Cementitious Composite (ECC), and Ultra High-Performance Concrete (UHPC), two shear span lengths, three reinforcement ratios, and six axial load levels were investigated in this study. The numerical framework implemented is described in the following subsections.

# 3.1. Modeling setup

Fig. 2 presents an overview of the numerical models implemented in this study. The column geometries were selected to represent the scale of a future experimental program to be undertaken at the New Jersey Institute of Technology. Therefore, section dimensions of 130 mm  $\times$  180 mm were selected. Two shear span lengths of 650 mm and 1080 mm corresponding to an aspect ratio of 3.6 and 6, respectively, were selected in order to investigate the effects of changing moment gradients and shear demand. A foundation beam with dimensions  $130~\text{mm}\times380~\text{mm}\times800~\text{mm}$  was provided. Linear elastic steel plates were modeled at the foundation beam anchorage and column load points to avoid concentrated damage. Subsequently, the steel plates, columns, and foundation beams were discretized into  $10~\text{mm}\times10~\text{mm}$  eight-node quadrilateral elements.

The columns were symmetrically reinforced with either 10, 13, or 16 mm Grade 420 mild longitudinal steel equating to a tension reinforcement ratio,  $A_{s\,ten}/bh$ , of 0.6%, 1.1%, and 1.7%, respectively. A number of studies investigating the effects of transverse reinforcement ratio on beam and column responses have demonstrated the potential to reduce or even eliminate transverse reinforcement due to the shear contributions of fibers while maintaining flexural failure mechanisms [7, 35,36]. However, work by Hung et al. [37] demonstrated the potential negative impacts on post-peak ductility from varying transverse reinforcement ratios. Since no consensus has been reached on the minimum transverse reinforcement required, a transverse reinforcement ratio,  $A_{sh}/bs$ , of 0.18% corresponding to the ACI 318-19 [38] minimum was provided and fixed cross all models. Moreover, based on conservative

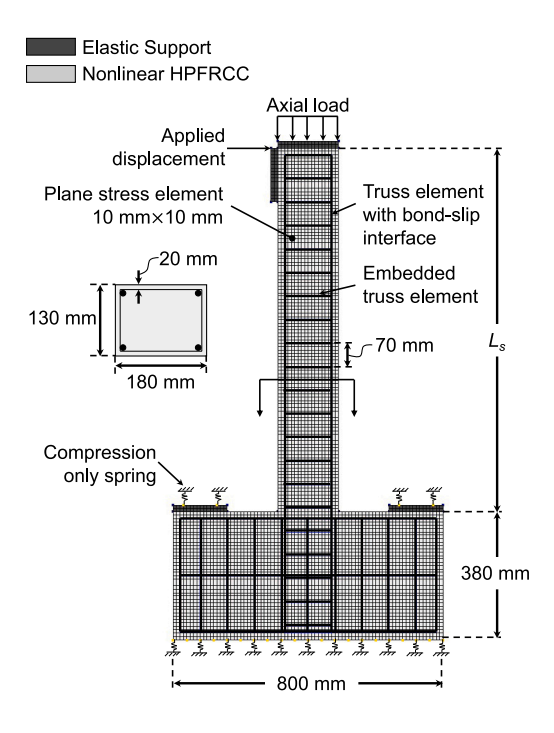


Fig. 2. Overview of finite element modeling setup.

shear capacity estimations [7], the shear demand to capacity ratio of the numerically simulated columns ranged from 17% to 75% with an average of 32%, well under unity. Therefore, diagonal cracking, typically associated with high shear deformations was not observed in the numerical simulation results with this transverse reinforcement detailing. The transverse reinforcement was subsequently discretized into 10 mm embedded truss elements. Bond–slip interfaces between the longitudinal reinforcement and HPFRCC material were additionally modeled and are further discussed in Section 3.2.

## 3.2. Constitutive material models and properties

To date, a number of HPFRCC material mixtures have been developed based on varying material design philosophies, material constituents, and structural applications [3,4,39,40]. Notably, ECC, UHPC, and HyFRC have garnered increasing research interest in various structural applications (e.g., beams, columns, and in-fill panel retrofits) highlighted by several large-scale experimental tests [8,35,41,42]. ECC, based on micromechanical principles and appropriate fiber-matrix tailoring [4,39], has been proposed for use in high shear applications [35, 41] due to its' fine multi-micro cracking behavior and high tensile ductility. Composed primarily of a cementitious matrix with no coarse aggregate and polyvinyl alcohol fibers, ECC has been reported to have tension and compression strengths in the range of 2.6-5 MPa and 30-90 MPa [39,43], respectively. UHPC, designed based on particle packing theory, exhibits characteristically high compressive strengths ranging from 112-210 MPa and tensile strengths ranging from 5-12 MPa [3,5,44]. Owed to its high compression and tension ductility, UHPC has been extensively deployed in structural applications (i.e., flexural components) within research [8,17,32,36,37,45] as well some nonstructural applications in industry (e.g., closure bridge joints). HyFRC, designed to largely parallel normal strength concrete mixtures with the addition of optimized fiber lengths [40], has been proposed for improving the seismic resiliency of structures [42]. HyFRC tension and compressive strengths have been reported to range between 1.5-3.1 MPa and 31.5-45 MPa, respectively [46-48].

In this study, all three materials, ECC, UHPC, and HyFRC, were selected for further investigation to quantify the effects of material properties of relevant HPFRCC materials on a component's plastic hinge length. Past investigations into the material-level response of ECC and UHPC have highlighted their strong dependency on material composition (e.g., type of fibers and proportion of dry constitutive materials) and testing method [3,5]. Further, work by Gencturk and Elnashai [11] demonstrated the impact of ECC tensile stress-strain variability on a component's response. It was found that component-level ductility could increase by as much as 120% due to increases in material-level ductility. However, due to the high computational costs associated with the employed high-fidelity models and the increase in the number of simulated beam-column elements necessary to account for materiallevel uncertainty, the employed material properties were strategically selected from the literature [17,39,44,46]. The representative material properties for ECC and HyFRC were selected based on the mean values of experimental tests [39,46]. UHPC1, UHPC2, and UHPC3 properties were selected as lower bound experimental values [44] and mean values containing various fiber volume percentages [17], respectively. Material properties are summarized in Table 2 and used to derive the material responses shown in Fig. 3a and b.

The tensile stress–strain envelope of Fig. 3a is a trilinear idealization characterized by a linear elastic state followed by a strain hardening and softening state [32]. In order to account for the softening behavior of HPFRCCs during cracking, a total strain-based smeared crack formulation with a fixed crack orientation was adopted. As a result of using smeared crack approaches, the tension and compression softening states were normalized by fracture energies as well as the crack bandwidth, h, which is taken as the square root of the element area. A compression model developed by Shao et al. [32] was employed in this study (see Fig. 3b). The model is characterized by a linear elastic state, quadratic state up to  $f_c'$ , followed by a softening and residual state. The residual strength was selected as a median value of  $0.20f_c'$  based on experimentally observed residual capacities [32,49] and therefore, implicitly accounts for transverse reinforcement and fiber confining effects.

Previous studies investigating the tension-stiffening effect of HPFRCC materials have highlighted the impact of bond strength on the spread of plasticity in reinforcing bars and ultimate drift capacities in components [31,48,50]. To capture the effects of bond strength and tension stiffening, bond–slip laws developed by Bandelt and Billington [30,51] were implemented for ECC and HyFRC materials while a bond–slip law developed by Shao et al. [33] (see Fig. 3c) was implemented for UHPC materials. In the case of the adopted UHPC mixtures in this study, the calculated maximum bond stresses were adjusted according to the reported 8%–11% reduction in the peak bond stress by Shao et al. [33] when fiber volume percentages were reduced from 2% to 1%. Lastly, steel reinforcement properties obtained from the literature [16] and also summarized in Table 2 were implemented in a Von Mises plasticity model as shown in Fig. 3d.

### 3.3. Boundary conditions and analysis parameters

To capture the stiffness of physical testing constraints, compression-only springs were modeled at the foundation beam base and steel anchorage plates in lieu of pinned constraints. Loading of the column was accomplished in two stages. Stage one entailed the application of a distributed line load corresponding to an axial load level,  $P/A_g f_c'$ , of 0%, 5%, 10%, 15%, 20%, or 25%. Stage two consisted of a laterally applied displacement of 0.25 mm in a stepwise manner until column failure.

Solving of equilibrium was accomplished using a Newton–Raphson method with a line-search algorithm. Each iterative step was considered converged if a displacement norm of 0.1%, force norm of 1%, and energy norm of 0.01% were satisfied.

**Table 2** HPFRCC and steel reinforcement material properties.

Description	Notation	Unit	HyFRC	ECC	UHPC 1a	UHPC 2 <sup>b</sup>	UHPC 3 <sup>c</sup>	Longitudinal steel	Transverse steel
Modulus of elasticity	E	GPa	17.2	18.5	40.3	50.4	50.2	200	205
Poisson's ratio	υ	mm/mm	0.15	0.15	0.18	0.18	0.18	0.30	0.30
Shear retention factor	$\beta_s$	%	1	1	1	1	1	_	_
Compressive strength	$f_c'$	MPa	45	55	120	187.8	185.8	-	-
Strain at peak compressive stress	$\epsilon_{cp}$	%	0.44	0.49	0.38	0.43	0.43	-	-
Compressive fracture energy	$G_c$	MPa/mm	61	138	180	180	180	-	-
Tensile strength	$f_t$	MPa	1.8	2.9	8	7.2	10.5	-	-
Strain at crack localization	$\epsilon_{tp}$	%	0.30	0.75	0.20	0.18	0.20	_	_
Tensile fracture energy	$G_f$	MPa/mm	5.3	6.1	19	11.6	20	_	_
Slip at onset of softening	S <sub>max</sub>	mm	1	1	_	_	_	_	_
Bond-slip post peak stiffness	k	MPa/mm	1	1	-	-	_	-	-
Yield stress	$f_{v}$	MPa	_	-	-	-	-	455	690
Strain at onset of hardening	$\epsilon_{sh}$	%	_	-	_	_	_	0.02	_
Ultimate strain	$\epsilon_{su}$	%	_	-	_	_	_	0.18	-
Ultimate stress	$f_u$	MPa	-	-	-	-	-	675	-

<sup>&</sup>lt;sup>a</sup> Fiber volume fraction of 1.5%.

c Fiber volume fraction of 2%.

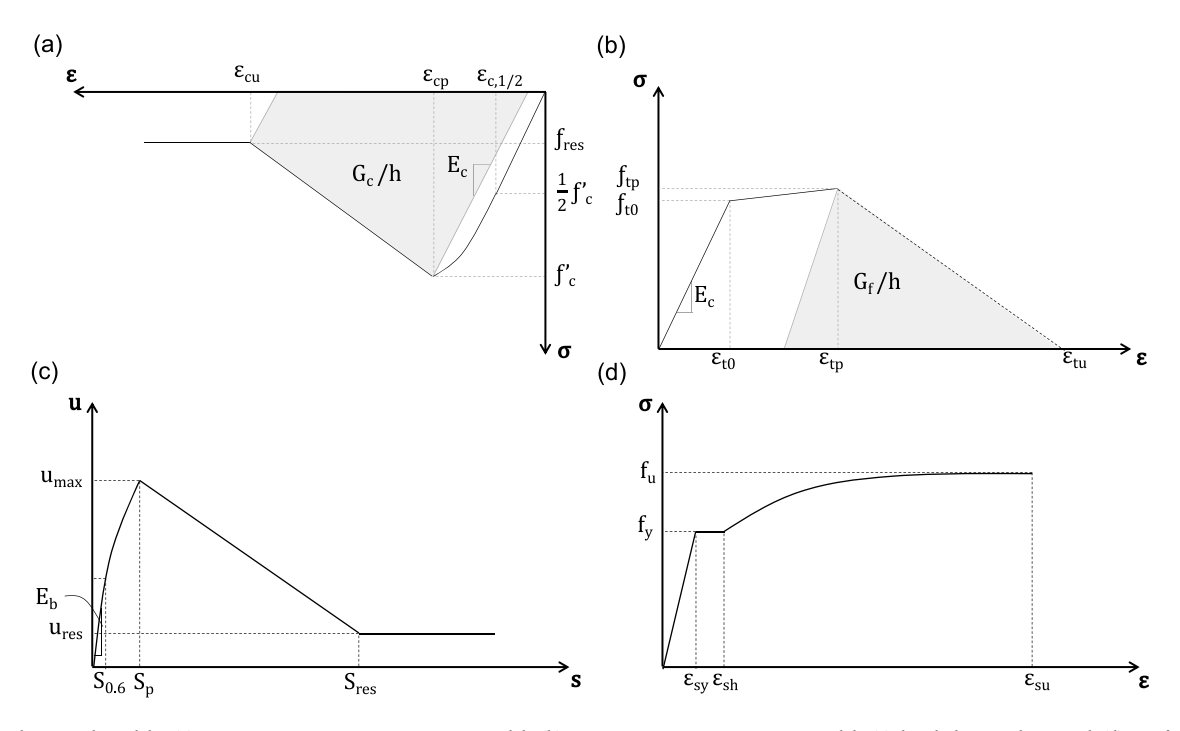


Fig. 3. Uniaxial material models: (a) HPFRCC compressive stress-strain model, (b) HPFRCC tension stress-strain model, (c) bond-slip envelope, and (d) reinforcement steel stress-strain model.

# 4. Numerical results and discussion

In the following subsections, the damage patterns and plastic hinge length trends of the numerical simulations are presented in order to highlight and inform the development of the plastic hinge length expressions discussed in Section 5.

# 4.1. Influence of axial load and material properties on damage and curvature distribution

Principle tensile strain contours and curvature distributions are presented in Fig. 4a–h for representative ECC and UHPC1 simulations at the collapse level of each model. These results will inform the plastic hinge length trends identified in Section 4.2 and give insight into the spread of damage in HPFRCC columns. The selected group columns have a shear span of 1080 mm, a tension reinforcement ratio of 1.10%, and an axial load level ranging between 0% to 20%.

Initial observation of the principle tensile strain contours of Fig. 4a (ECC column with 0% axial load) reveals the formation of two localized cracks above and below the column interface with softening damage (i.e., the yellow contours), associated with fiber pullout and/or rupture, penetrating across the majority of the cross-section. As the axial load level increases to 10% in Fig. 4b, softening damage distributes to a lesser degree across the column span and cross-section. Similar to Fig. 4a, two localized cracks form again. Further increasing the axial load to 20% as shown in Fig. 4c results in softening damage distributing across the entire base of the column implying a combination of horizontal damage from flexure and, to a larger degree, vertical damage from the axial load.

To quantify the spread of damage previously presented, the curvature distribution as well as the length over which curvature concentrates is plotted in Fig. 4d and overlaid in Fig. 4a-c, respectively. Section curvatures are calculated using Eq. (5) on the assumption that plane sections remain plane. In addition, the length over which the

b Fiber volume fraction of 1%.

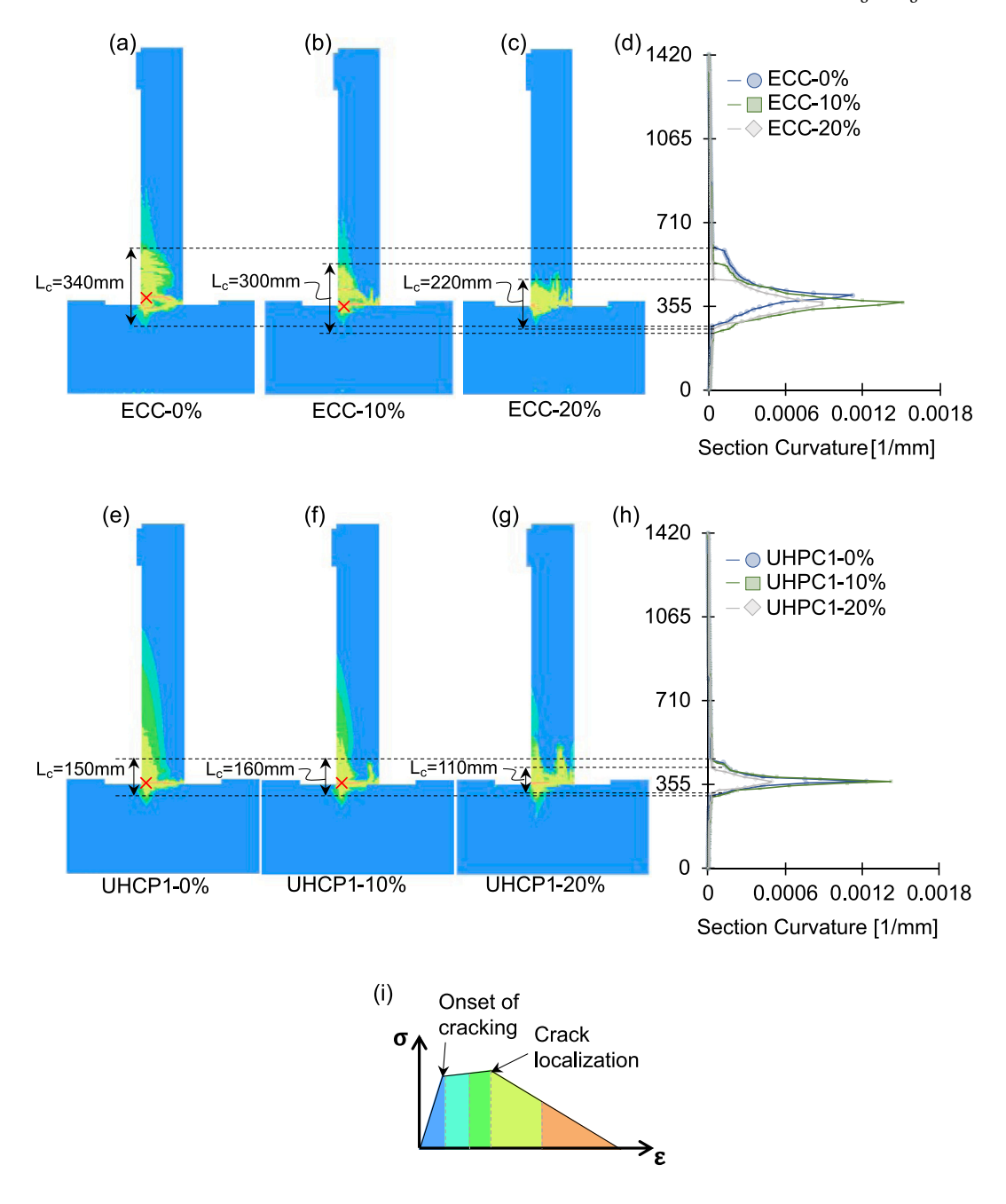


Fig. 4. Principle tensile strain contours and curvature distributions of ECC and UHPC1 columns at varying axial load levels at collapse level. Notation (HPFRCC-axial load), (a) ECC-0%, (b) ECC-10%, (c) ECC-20%, (d) ECC curvature distribution along column, (e) UHPC1%-0%, (f) UHPC1%-10%, (g) UHPC1%-20%, (h) UHPC1 curvature distribution along column, and (i) principle tensile strain contour key. (For interpretation of the references to color in this figure legend, the reader is referred to the web version of this article.)

curvature concentrates,  $L_c$ , is determined as the length over which curvature exceeds the yield curvature. As shown in Fig. 4a–d the curvature concentration length decreases from 340 mm at 0% axial load to 200 mm at 20% axial load, confirming the previously observed damage pattern trends.

The effects of HPFRCC tensile strength on the spread of damage and curvature distribution are established when comparing Fig. 4a–d and Fig. 4e–h. In comparison to the two localized cracks reported for the ECC columns at 0% and 10% axial load, only one localized crack formed in the UHPC1 columns at the same load levels. In addition, the curvature concentration lengths of the UHPC1 and ECC columns show that the higher tensile strength of UHPC1 ( $f_t = 8$  MPa) results in a curvature concentration length nearly half that of ECC ( $f_t = 2.8$  MPa).

For example, the curvature concentration length of the UHPC1 column in Fig. 4e is 150 mm in comparison to 340 mm in the ECC column of Fig. 4a. These results can simply be explained through experimental tension stiffening tests conducted by Moreno et al. [48] where an increase in HPFRCC tensile strength for the same reinforcement ratio resulted in fewer splitting and transverse cracks. This reduction is caused by the increased toughness of higher HPFRCC tensile strengths resulting in a smaller gage length in which the reinforcement strain concentrates.

It is noted that in the 0% and 10% axial load cases for both ECC and UHPC1 columns, the mode of failure is observed to be reinforcement rupture (i.e., the tension reinforcement reaching 18% strain) and is denoted by the  $\times$  symbol. Further increases to 20% axial load result

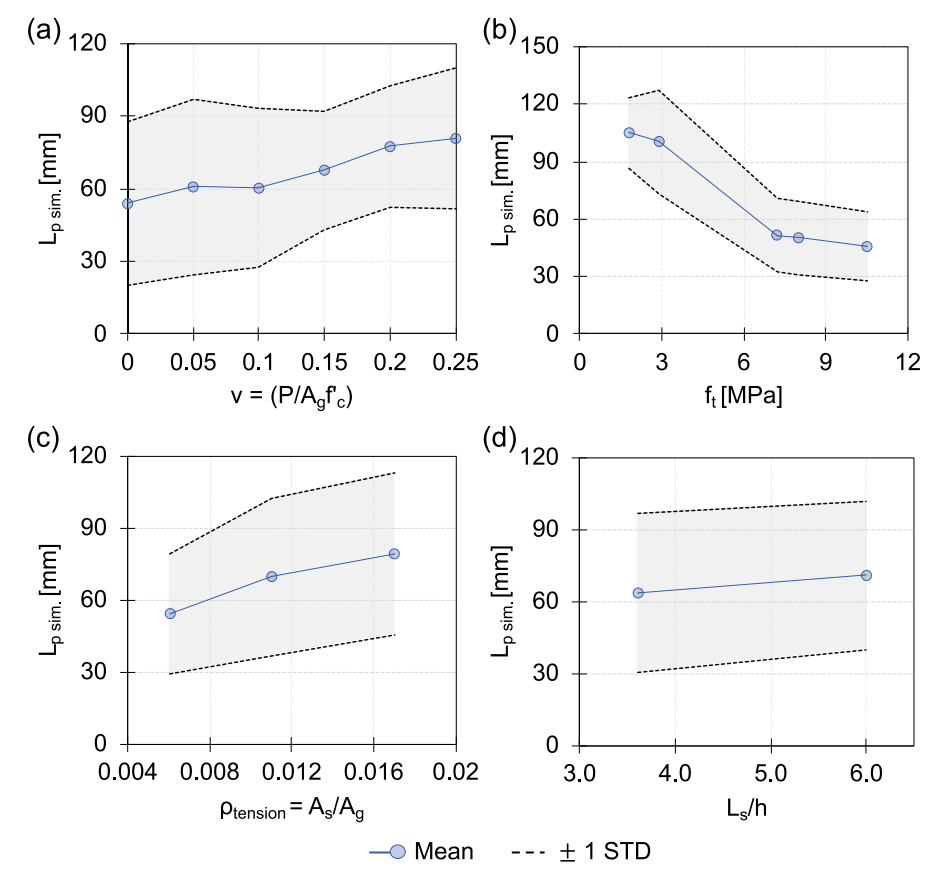


Fig. 5. Trends in the plastic hinge length vs. (a) axial load level, (b) HPFRCC tensile strength, (c) tension reinforcement ratio, and (d) column aspect ratio.

in compression failure (i.e., a 20% loss of lateral load capacity) and thus imply a transition in failure mechanism between 10% and 20% axial load. While the predominate failure mode of HPFRCC columns observed in the literature is a loss of 20% lateral load carrying capacity [7,36,37,52], reinforcement fracture has been observed in several experimental columns at low axial load levels (i.e., 5%–10%) [8,9,36].

#### 4.2. Influence of axial load level on plastic hinge length

Using the yield and ultimate failure criteria outlined in Section 2.1, the critical rotations ( $\theta_y$  and  $\theta_u$ ) and section curvatures ( $\phi_y$  and  $\phi_u$ ) – determined from Eq. (5) – were used to determine each component's plastic hinge length using Eq. (4). The mean and standard deviation responses of the calculated plastic hinge lengths across various design parameters are presented in Fig. 5a–d.

As discussed in Section 2.2, the effects of axial load on plastic hinge length have been subject to debate in structural elements with ordinary concrete. To investigate the plastic hinge length dependency on axial load levels, the mean plastic hinge length versus axial load level for all numerically simulated columns is plotted in Fig. 5a. As can be observed, the relative increase in plastic hinge length from 0% to 10% is marginal (i.e., below a 13% increase in plastic hinge length). However, further increases in the axial load level, from 10% to 25%, resulted in a clear linear increase in plastic hinge length. Combining the observed shift from tension to compression failure at axial load levels between 10% and 20% reported in Section 4.1 and the results of Fig. 5a suggest that the effects of axial load on plastic hinge length are failure mode dependent. Thus, plastic hinge length expressions for HPFRCC components exhibiting tension failure mechanisms would not be functions of axial load in contrast to components exhibiting compression failure mechanisms.

In addition, the results of Section 4.1 and Fig. 5a, may further explain the similarly observed trends reported by Bae et al. [23] in reinforced concrete columns, where up to an axial load level of 20%, the plastic hinge length of reinforced concrete columns remain unaffected by the axial load.

# 4.3. Influence of reinforcement ratio and material tensile strength on plastic hinge length

Previous studies investigating the plastic hinge length and rotation capacity of HFPRCC beams have reported and emphasized the inverse relationship between reinforcement ratio and HPFRCC tensile strength [17,18,50]. The results of Fig. 5b-c further support such findings. For instance, as shown in Fig. 5b, an increase in the HPFRCC tensile strength from 1.8 MPa to 10.5 MPa resulted in a 56% reduction in the plastic hinge length. In contrast, an increase in the tension reinforcement ratio from 0.61% to 1.7% resulted in a 45% increase in plastic hinge length as shown in Fig. 5c. This inverse behavior, largely attributed to tension stiffening effects, suggests that lower HPFRCC tensile strengths are favorable for longer plastic hinge lengths and therefore, higher component rotation capacity. However, in the context of combined axially and laterally loaded components, adequate tensile strengths for a given HPFRCC material should be provided to ensure appropriate shear capacity while avoiding spalling and other deleterious behavior that may affect the plastic hinge length.

# 4.4. Influence of shear span length on plastic hinge length

In establishing the influence of moment gradient and shear demands on plastic hinge length, the shear span length was normalized to the column section height and plotted in Fig. 5d. It can be observed that a near doubling of shear span length only increases the plastic

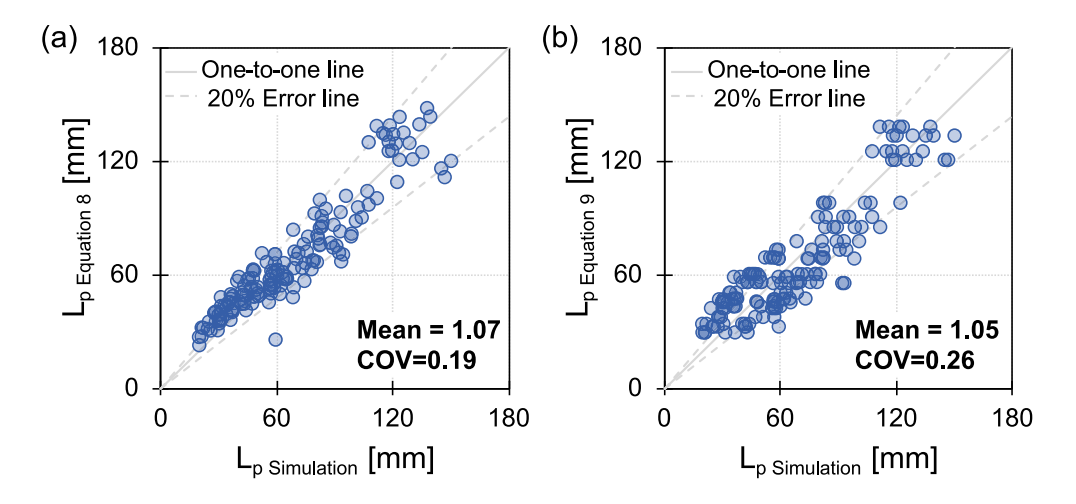


Fig. 6. Predictive performance of (a) Eq. (8) and (b) Eq. (9) against plastic hinge lengths calculated from the simulations.

hinge length by 11% which is in line with previously developed expressions [18,19,22,28]. Further, these findings suggest that changes in moment gradient and shear demand have minimal impact on a column's plastic hinge length provided that the component exhibits a flexural failure mechanism – achieved through modern design provisions – and low shear demand to capacity (i.e., below 50%). It is noted that previous plastic hinge length studies including this study are based on flexure-dominated components. Thus, the effects of shear span length may be more pronounced in poorly detailed or shear-dominant components due to the opening of large diagonal tension cracks. Future investigations into columns subjected to high shear demand to capacity ratios are warranted.

#### 5. Calibration of plastic hinge length expressions

In establishing the numerical database for expression calibration, 164 of 180 simulations were used for data analysis, and 16 of 180 simulations were omitted due to convergence issues and observed reinforcement pullout. Selection of the plastic hinge length functional form presented in Eqs. (6) and (7) was based on the past expressions summarized in Table 1 and the trends presented in Fig. 5a–d. While the two proposed equations are nearly identical, Eq. (6) explicitly accounts for axial load with a variable, while Eq. (7) implicitly accounts for axial load through its calibrated coefficients. It is noted that in Fig. 5a, the effects of axial load on plastic hinge length are contingent on whether the component exhibits a tension or compression failure mechanism. However, in order to avoid unnecessarily complex criteria for the use of the proposed expressions, all 164 simulations were used in the calibration of expression coefficients without regard to the failure mechanism.

$$L_{p} = \beta_{0} + \beta_{1} L_{s} + \beta_{2} \frac{\rho f_{y}}{f_{t}} + \beta_{3} v$$
 (6)

$$L_{p} = \beta_{0} + \beta_{1} L_{s} + \beta_{2} \frac{\rho f_{y}}{f_{s}}$$
 (7)

The first term of Eqs. (6) and (7), shear span length,  $L_s$ , is proposed in order to account for the effects of moment gradient on the flexural and shear deformations. The second term,  $\rho f_y/f_t$ , is proposed to account for the inverse effects of reinforcement ratio and HPFRCC tensile strength on the fixed-end rotations. In this study,  $\rho$  is defined as  $(A_s/A_g)*100$  where  $A_s$  is the effective tension reinforcement area (i.e., the area of reinforcement acting in tension which may include the extreme tension reinforcement and part of the web reinforcement) and  $A_g$  is the gross

cross-sectional area. The third term of Eq. (6) is proposed to account for the effects of axial load where v is  $(P/f'_{c}A_{v}) * 100$ .

The  $\beta$  coefficients were determined by minimizing the sum of squares leading to the following proposed expressions:

$$(SI): L_p = 0.02L_s + 0.37 \frac{\rho f_y}{f_t} + 0.94v$$
 
$$(Imperial): L_p = 0.02L_s + 0.015 \frac{\rho f_y}{f_t} + 0.037v$$
 (8)

$$(SI): L_{p} = 0.03L_{s} + 0.38 \frac{\rho f_{y}}{f_{t}}$$
 (9) 
$$(Imperial): L_{p} = 0.03L_{s} + 0.015 \frac{\rho f_{y}}{f_{t}}$$

The resulting predictive performance of Eqs. (8) and (9) against simulated data is presented in Fig. 6a and b. Eq. (8) has a mean predicted-to-simulated ratio of 1.07 with a coefficient of variation (COV) of 19% indicating reasonable levels of agreement with the simulated data. Eq. (9), implicitly accounting for axial load, has a mean predicted-to-simulated ratio of 1.05 with a COV of 26% indicating that at the expense of higher scatter, relative predicting accuracy can be maintained.

## 6. Experimental verification and discussion

In validating the predictive performance of the plastic hinge length expressions developed in this study and those proposed by others, an experimental database comprised of 47 components from the literature was compiled. The experimental database, presented in Table 3, is composed of 19 columns and 28 beams of which 28 of the components were tested under monotonic loading and 19 under quasi-static cyclic loading. Further, the database covers a range of cross-section geometries, reinforcement ratios, material properties, axial load levels, and failure mechanisms.

Section curvature analysis using an open-source finite element analysis program, OpenSees [53], was used to calculate each component's analytical section curvature. Component sections were modeled and discretized into uniaxial fibers where the fiber stress–strain behavior was associated with an HPFRCC or steel material model. In particular, the Pinching4 material model was used to reconstruct a multi-linear representation of the HPFRCC tension and compression response outlined in Section 3.2. A Dodd-Restrepo model was used for modeling the steel stress–strain behavior. Table 3 presents select material properties used in the section analysis from their respective studies. In the event

Experimental database

Reference	Specimen ID	Material	Component	Loading	Failure no.	L <sub>s</sub> [mm]	b [mm]	h [mm]	$\rho_{ten.}$	$\rho_{web.}$	$\rho_{comp.}$	E <sub>c</sub> [GPa]	f' <sub>c</sub> [MPa]	f, [MPa]	$E_s$ [GPa]	f <sub>y</sub> [MPa]	f <sub>u</sub> [MPa]	ε <sub>su</sub> [%]	ν	Δ <sub>y</sub> [mm]	Δ <sub>u</sub> [mm]	M <sub>y</sub> [kN-m]	M <sub>u</sub> [kN-m]
Hung et al. [37]	H5T0-F150	UHPC	Column	Monotonic	2	1200	200	200	0.015	0.010	0.015	37.7ª	105.0	9.2	199.5	439.0	630	13.6	0.06	20.9	141.6	65.4	82.4
	H5T5-F75	UHPC	Column	Monotonic	2	1200	200	200	0.015	0.010	0.015	37.7ª	105.0	5.1	199.5	439.0	630	13.6	0.07	20.8	63.4	66.6	74.2
	H10T0-F150	UHPC	Column	Monotonic	2	1200	200	200	0.015	0.010	0.015	37.0ª	101.0	7.1	199.5	439.0	630	13.6	0.07	20.3	118.3	63.6	83.2
	H10T10-F150	UHPC	Column	Monotonic	2	1200	200	200	0.015	0.010	0.015	37.5ª	104.0	6.7	199.5	439.0	630	13.6	0.06	21.1	102.2	58.7	70.0
Li et al. [52]	ECC06	ECC	Column	Monotonic	2	400	120	120	0.004	0.000	0.004	21.0	54.0	6.0	185.8	450.0	-	18.0	0.13	2.5	6.8	7.8	7.2
	ECC08	ECC	Column	Monotonic	2	400	120	120	0.007	0.000	0.007	21.0	54.0	6.0	185.8	450.0	-	18.0°	0.16	3.0	7.0	9.8	9.3
	ECC10	ECC	Column	Monotonic	2	400	120	120	0.011	0.000	0.011	21.0	54.0	6.0	185.8	450.0	_	18.0°	0.20	3.3	9.2	12.5	11.3
	ECC12	ECC	Column	Monotonic	2	400	120	120	0.016	0.000	0.016	21.0	54.0	6.0	185.8	450.0	_	18.0°	0.26	4.1	7.4	16.4	14.0
	ECC14	ECC	Column	Monotonic	2	400	120	120	0.021	0.000	0.021	21.0	54.0	6.0	185.8	450.0	_	18.0°	0.32	4.8	6.8	20.4	17.1
Yoo and Yoon [45]	S13-0.94%	UHPC	Beam	Monotonic	1	900	150	220	0.008	0.000	0.005	46.7	211.8	5.8	200.0	495.0	743	19.0	0.00	12.3	52.2	36.3	31.3
10011 [40]	S13-1.50%	UHPC	Beam	Monotonic	1	900	150	220	0.012	0.000	0.005	46.7	211.8	5.8b	200.0	510.0	765	19.0	0.00	15.3	51.3	49.5	44.5
	S19-0.94%	UHPC	Beam	Monotonic	1	900	150	220	0.008	0.000	0.005	46.9	209.7	8.5 <sup>b</sup>	200.0	495.0	743	19.0	0.00	12.1	50.4	35.1	33.3
	S19-1.50%	UHPC	Beam	Monotonic	1	900	150	220	0.000	0.000	0.005	46.9	209.7	8.5 <sup>b</sup>	200.0	510.0	765	19.0	0.00	12.1	65.7	46.5	44.8
	S30-0.94%	UHPC	Beam	Monotonic	1	900	150	220	0.008	0.000	0.005	46.8	209.7	8.0 <sup>b</sup>	200.0	495.0	743	19.0	0.00	12.3	80.1	36.0	34.3
	S30-1.50%	UHPC	Beam	Monotonic	1	900	150	220	0.008	0.000	0.005	46.8	209.7	8.0 <sup>b</sup>	200.0	510.0	765	19.0	0.00	13.8	72.9	47.4	44.5
	T30-0.94%	UHPC	Beam	Monotonic	1	900	150	220	0.008	0.000	0.005	47.0	232.1	9.5 <sup>b</sup>	200.0	495.0	743	19.0	0.00	12.3	65.7	35.1	34.3
	T30-1.50%	UHPC	Beam	Monotonic	1	900	150	220	0.008	0.000	0.005	47.0	232.1	9.5 <sup>b</sup>	200.0	510.0	765	19.0	0.00	13.3	81.9	50.4	48.1
Bandelt and Billington [16]	M-0.54	ECC	Beam	Monotonic	1	457	130	230	0.005	0.000	0.005	17.8ª	47.0	2.2 <sup>b</sup>	197.5	395.0	620	18.0	0.00	4.2	50.3	15.9	15.9
	M-0.70	ECC	Beam	Monotonic	1	685	130	180	0.007	0.000	0.007	17.8ª	47.0	2.2b	202.3	445.0	690	18.0	0.00	6.1	57.5	14.4	14.8
	M-1.3	ECC	Beam	Monotonic	1	685	130	180	0.011	0.000	0.011	17.8ª	47.0	2.2 <sup>b</sup>	197.8	455.0	675	16.0	0.00	8.3	82.2	22.2	25.3
	M-2.0	ECC	Beam	Monotonic	1	685	130	180	0.017	0.000	0.017	17.8ª	47.0	2.2 <sup>b</sup>	200.0	440.0	625	15.0	0.00	8.8	109.6	30.8	38.8
Shao and Billington [17]	Ductal-vf2.0-ρ0.96	UHPC	Beam	Monotonic	2	800	150	220	0.008	0.000	0.008	50.2ª	185.8	10.5 <sup>b</sup>	200.0°	475.0	783	18.0°	0.00	6.5	24.6	44.6	37.9
	Ductal-vf1.0-ρ0.96	UHPC	Beam	Monotonic	1	800	150	220	0.008	0.000	0.008	50.1ª	185.3	7.0 <sup>b</sup>	200.0°	475.0	783	18.0°	0.00	6.6	41.6	34.9	30.3
	Ductal-vf0.50-ρ0.96	UHPC	Beam	Monotonic	2	800	150	220	0.008	0.000	0.008	49.5ª	181.0	4.0 <sup>b</sup>	200.0°	475.0	783	18.0°	0.00	5.4	55.3	28.3	30.6
	Ductal-vf2.0-ρ2.10	UHPC	Beam	Monotonic	1	800	150	220	0.017	0.000	0.017	50.2ª	185.8	10.5 <sup>b</sup>	200.0°	475.0	783	18.0°	0.00	6.8	69.1	63.5	64.9
	Ductal-vf1.0-ρ2.10	UHPC	Beam	Monotonic	1	800	150	220	0.017	0.000	0.017	50.1ª	185.3	7.0 <sup>b</sup>	200.0°	475.0	783	18.0°	0.00	7.8	71.8	57.1	63.8
	UP-F-vf2.0-ρ2.10	UHPC	Beam	Monotonic	1	800	150	220	0.017	0.000	0.017	47.8ª	169.0	9.0 <sup>b</sup>	200.0°	475.0	783	18.0°	0.00	7.9	80.2	63.3	60.0
	UP-F-vf1.0-ρ2.10	UHPC	Beam	Monotonic	1	800	150	220	0.017	0.000	0.017	47.7ª	168.2	5.0 <sup>b</sup>	200.0°	475.0	783	18.0°	0.00	7.8	77.8	57.5	60.5
Wu et al. [7]	C5	ECC	Column	Cyclic	2	525	300	300	0.007	0.000	0.007	22.2	45.0	4.4	200.0°	498.0	_	18.0°	0.17	3.1	26.1	204.7	221.4
()	C6	ECC	Column	Cyclic	2	525	300	300	0.007	0.000	0.007	22.2	45.0	4.4	200.0°	498.0	_	18.0°	0.09	2.6	33.1	126.1	126.7
	C7	ECC	Column	Cyclic	2	525	300	300	0.007	0.000	0.007	22.2	45.0	4.4	200.0°	498.0	_	18.0°	0.09	2.6	29.0	113.5	118.0
Marchand et al. [36]	U1-S-HL-A	UHPC	Column	Cyclic	2	1200	160	200	0.007	0.000	0.007	62.5	220.2	12.9	188.4	532.1	590.5	6.4	0.16	10.0	26.2	84.5	97.2
	U2-S-HL-A	UHPC	Column	Cyclic	2	1200	160	200	0.007	0.000	0.007	62.1	222.5	14.3 <sup>b</sup>	188.4	532.1	590.5	6.4	0.16	11.1	26.1	88.5	96.9
	U1-NS-HL-A	UHPC	Column	Cyclic	2	1200	160	200	0.007	0.000	0.007	62.5	220.2	12.9b	188.4	532.1	590.5	6.4	0.16	10.9	26.1	86.5	102.4
	U1-S-RL-A-a	UHPC	Column	Cyclic	2	1200	160	200	0.007	0.000	0.007	62.5	220.2	12.9 <sup>b</sup>	188.4	532.1	590.5	6.4	0.09	8.7	29.6	64.5	68.0
	U1-S-RL-A-b	UHPC	Column	Cyclic	2	1200	160	200	0.007	0.000	0.007	62.5	220.2	12.9bb	188.4	532.1	590.5	6.4	0.09	8.7	29.2	64.5	74.6
	U2-S-RL-A	UHPC	Column	Cyclic	2	1200	160	200	0.007	0.000	0.007	62.1	222.5	14.3 <sup>b</sup>	188.4	532.1	590.5	6.4	0.09	8.7	21.4	64.5	74.6
	U2-NS-RL-A	UHPC	Column	Cyclic	2	1200	160	200	0.007	0.000	0.007	62.1	222.5	14.3 <sup>b</sup>	188.4	532.1	590.5	6.4	0.09	8.7	21.4	64.5	77.4
Bandelt and	C-0.54	ECC	Beam	Cyclic	1	457	130	230	0.005	0.000	0.005	17.8ª	47.0	2.2 <sup>b</sup>	197.5	395.0	620	18.0	0.00	3.0	15.6	14.9	12.7
Billington [16]	C-0.70	ECC	Beam	Cyclic	1	685	130	180	0.007	0.000	0.007	17.8ª	47.0	2.2 <sup>b</sup>	202.3	445.0	690	18.0	0.00	5.4	32.9	14.0	14.7
	C-0.70 C-1.3	ECC	Beam	Cyclic	1	685	130	180	0.007	0.000	0.007	17.8°	47.0	2.2 <sup>b</sup>	197.8	455.0	675	16.0	0.00	8.7	58.2	19.7	22.3
Frank et al. [6]	ECC-0.73-F	ECC	Beam	Cyclic	1	760	127	178	0.007	0.000	0.007	7.0	44.0	4.0 <sup>b</sup>	200.0	445.0	690	18.0	0.00	7.4	64.6	11.8	13.2
[O]	ECC-0.95-F	ECC	Beam	Cyclic	1	813	165	203	0.008	0.000	0.008	7.0	44.0	4.0 <sup>b</sup>	200.0°	455.0	675	16.0	0.00	11.4	96.4	22.4	21.6
	ECC-1.0-F	ECC	Beam	Cyclic	1	813	165	203	0.008	0.000	0.008	7.0	44.0	4.0 <sup>b</sup>	200.0°	445.0	690	18.0	0.00	10.5	96.4	23.6	19.8
	ECC-1.0-F ECC-1.3-F	ECC	Beam	Cyclic	1	760	127	178	0.009	0.000	0.009	7.0	44.0	4.0 <sup>b</sup>	200.0°	455.0	675	16.0	0.00	10.5	90.4	19.2	22.0
	LCC-1.3-F	LUC	DCam	Cyclic				203		0.000	0.012												
	ECC-1.4-F	ECC	Beam	Cyclic	1	813	165		0.012			7.0	44.0	4.0 <sup>b</sup>	200.0°	455.0	675	16.0	0.00	17.3	137.4	33.1	26.8

Failure no. defined as.

Fracture of the tension reinforcement.
 20% drop in the lateral load carrying capacity

Determined from material model expressions [32]. Determined from inverse analysis

Assumed for analysis.

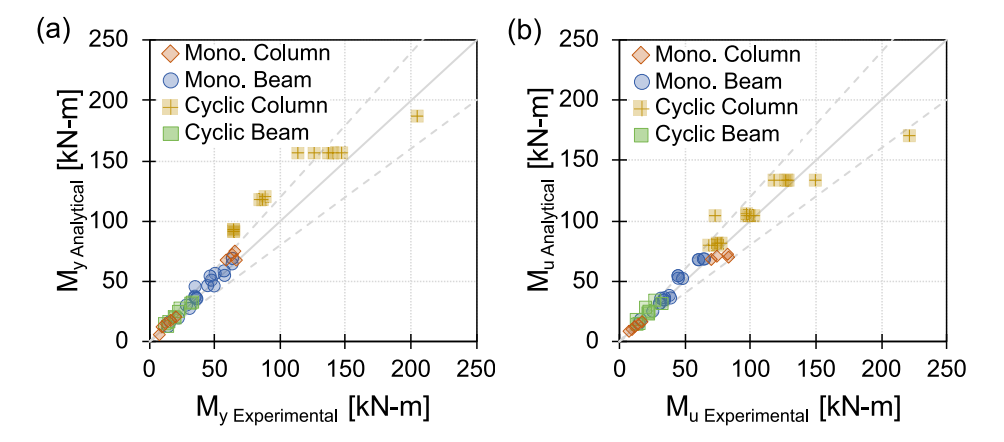


Fig. 7. Experimental versus analytically calculated moments at (a) yield and (b) ultimate displaced states.

that insufficient material data was reported in the physical experiment, material properties were estimated using modeling expressions and strain properties referenced in Section 3.2. Lastly, the yield and ultimate section curvatures were determined from the criteria outlined in Section 2.1.

Due to the limited reporting of experimental section curvatures, comparisons between experimental and analytically calculated curvatures could not be made. Instead, the corresponding yield and ultimate moments are compared to experimental values to gain insights into the validity of the analytical section curvatures. As presented in Fig. 7a and

**Table 4**Summary of prediction statistics of rotation capacities.

	Mono. Bea	am	Mono. Col	umn	Cyclic Bea	am	Cyclic Column		
	Mean	COV	Mean	COV	Mean	COV	Mean	COV	
$\theta_{y\ Theoretical}$	0.78	22%	1.02	33%	0.71	25%	1.94	37%	
$\theta_{u Eq. (8)}$	0.85	28%	0.98	37%	_	-	_	-	
$\theta_{u Eq. (9)}$	0.94	27%	0.97	41%	_	_	_	_	
$\theta_{u\ Pokhrel\ \&\ Bandelt}$	0.71	26%	0.92	40%	0.82	22%	1.15	32%	
$\theta_{u\ Wang\ et\ al}$ .	1.81	30%	1.42	34%	2.06	30%	1.85	28%	
$\theta_{u \ Tariq \ et \ al.}$	0.88	31%	0.70	31%	0.89	51%	0.86	23%	
θ <sub>u Pauley &amp; Priestly</sub>	3.12	36%	1.94	36%	2.54	31%	3.09	22%	
$\theta_{u \; Bae \; et \; al}$ .	0.85	32%	0.77	37%	0.83	48%	1.19	21%	
$\theta_{u\ Panagiotakos\ \&\ Fardis}$	2.14	39%	1.56	41%	1.95	34%	2.23	39%	

b, the calculated yield and ultimate moments have a mean predicted-to-simulated ratio of 1.10 and 1.07 and a COV of 15% and 12%, respectively, indicating a slight over-prediction of the component moments but overall strong agreement.

Following the calculation of each experimental component's moment-curvature response, the newly developed plastic hinge length expressions and those presented in Table 1 were used to estimate each component's ultimate rotation using Eq. (3). The resulting predicted to experimental rotation comparisons are shown in Fig. 8a-i with the corresponding summary of prediction statistics in Table 4. The prediction accuracy of the yield rotations, as presented in Fig. 8a and Table 4, is worth discussion as the yield rotations contribute on average 17% – based on Table 3 – to the ultimate rotation of a component. Upon analysis of Fig. 8a and Table 4, it can be observed that the assumed linear curvature distribution in Eq. (3) is shown to underpredict the yield rotation of monotonic and cyclic beams by 22%-29%, albeit with low scatter. In contrast, the linear assumption tends to overpredict yield rotations of cyclic columns by 94% with a high level of scatter. Reasons for the observed high scatter are largely due to the sensitivity of a component's yield rotation to the experimental setup as well as the simplifying assumptions of the curvature distribution made in Eq. (3). However, due to the relative simplicity of calculating the yield rotation and reasonable agreement with monotonic data, the assumption of Eq. (3) is maintained for further analysis of the component's ultimate rotation.

As shown in Fig. 8b and Table 4, Eq. (8) resulted in a mean predicted-to-simulated ratio of 0.98 and 0.85 and a COV of 37% and 28% for monotonic columns and beams respectively. The reason for the discrepancies between columns and beams is attributed to the calibration of the expression coefficients where ill-regard was taken to failure mechanism. Thus, it is likely that the coefficient for the axial load term closely matches that of compression failure components resulting in the underprediction of tension failure components. However, as shown in Fig. 8c and Table 4, Eq. (9) resulted in a mean predicted-to-simulated ratio of 0.97 and 0.95 and a COV of 41% and 27%, respectively. Thus, the prediction results of Eq. (9) imply the effects of axial load can largely be captured in the calculation of section curvature despite the dependency of plastic hinge length behavior on axial load and failure mechanism observed in Fig. 5a. In addition, it is noted that only a slight increase in scatter is observed when using Eq. (9) over the 10% increase reported in Section 5.

The monotonic prediction results of Eqs. (8) and (9) in comparison to those using expressions by others indicate a significant improvement in accuracy, particularly in beams. For example, the plastic hinge length expressions proposed by Pokhrel and Bandelt resulted in a mean predicted-to-simulated ratio of 0.71 and COV of 26% for beams in contrast to a mean predicted-to-simulated ratio of 0.94 and COV of 27% for Eq. (9). A marginal improvement is observed in Eq. (9) over that of Pokhrel and Bandelt for monotonic columns.

While the numerical simulations and expression calibrations have been limited to monotonic loading, insights into the validity of previously developed cyclic expressions and their predictive performance should be made considering the effects of axial load. Using cyclic plastic hinge expressions proposed by others (see Table 1) and the previously calculated section curvatures, the predicted ultimate rotations were calculated using Eq. (3) and are compared to the experimental HPFRCC beam and column rotations in Fig. 8d–i and Table 4. The results indicate that the plastic hinge length expressions developed by Pokhrel and Bandelt provide the highest prediction accuracy and lowest scatter for predicting the rotation capacity of cyclic beams. However, while the proposed cyclic expressions by Pokhrel and Bandelt [18] appear to overpredict the cyclic rotation of columns, the 15% overprediction is likely due to the reported overprediction of the yield rotations. Thus, improved yield rotation expressions are likely to more accurately demonstrate the predictive performance of the cyclic expressions developed by others.

#### 7. Limitations and future research

The capability of Eqs. (8) and (9) to predict experimental rotations was shown to be in good agreement as presented in Table 4 and Fig. 8 and an improvement over past expressions. However, several limitations exist, namely, the expressions are calibrated with components using mild longitudinal reinforcement and were not validated against experiments using high-strength reinforcement which has garnered increasing research attention in recent years for the deployment in HPFRCC components [9,54]. Issues may arise particularly in HPFRCC beams reinforced with high-strength steel as they have been shown to exhibit lower rotational capacities in comparison to components with mild longitudinal steel. Thus, the proposed monotonic expressions may potentially overestimate the rotation capacity of HPFRCC components reinforced with high-strength steel.

While the validity of the implemented finite element framework is well documented in beams, its extension to axially loaded components is less known, particularly accounting for material-level variability. This study shows that the employed framework works well with axially loaded members presented in the literature. Future research efforts validating the finite element framework against additional axially loaded HPFRCC components are underway by the second author with efforts to investigate the system-level performance of HPFRCC structures accounting for the effects of axial load using the developed plastic hinge length expressions.

#### 8. Conclusions

In summary, the effects of axial load, HPFRCC material properties, reinforcement ratio, and shear span length on the plastic hinge length of monotonically loaded beams and columns were investigated through 180 high-fidelity numerical simulations. Based on the numerical results, the equivalent plastic hinge length was found to be relatively insensitive to the axial load level of components experiencing tension failure. However, the equivalent plastic hinge length was found to be linearly dependent on the axial load for components exhibiting compression failure mechanisms. Additionally, the plastic hinge length of HPFRCC

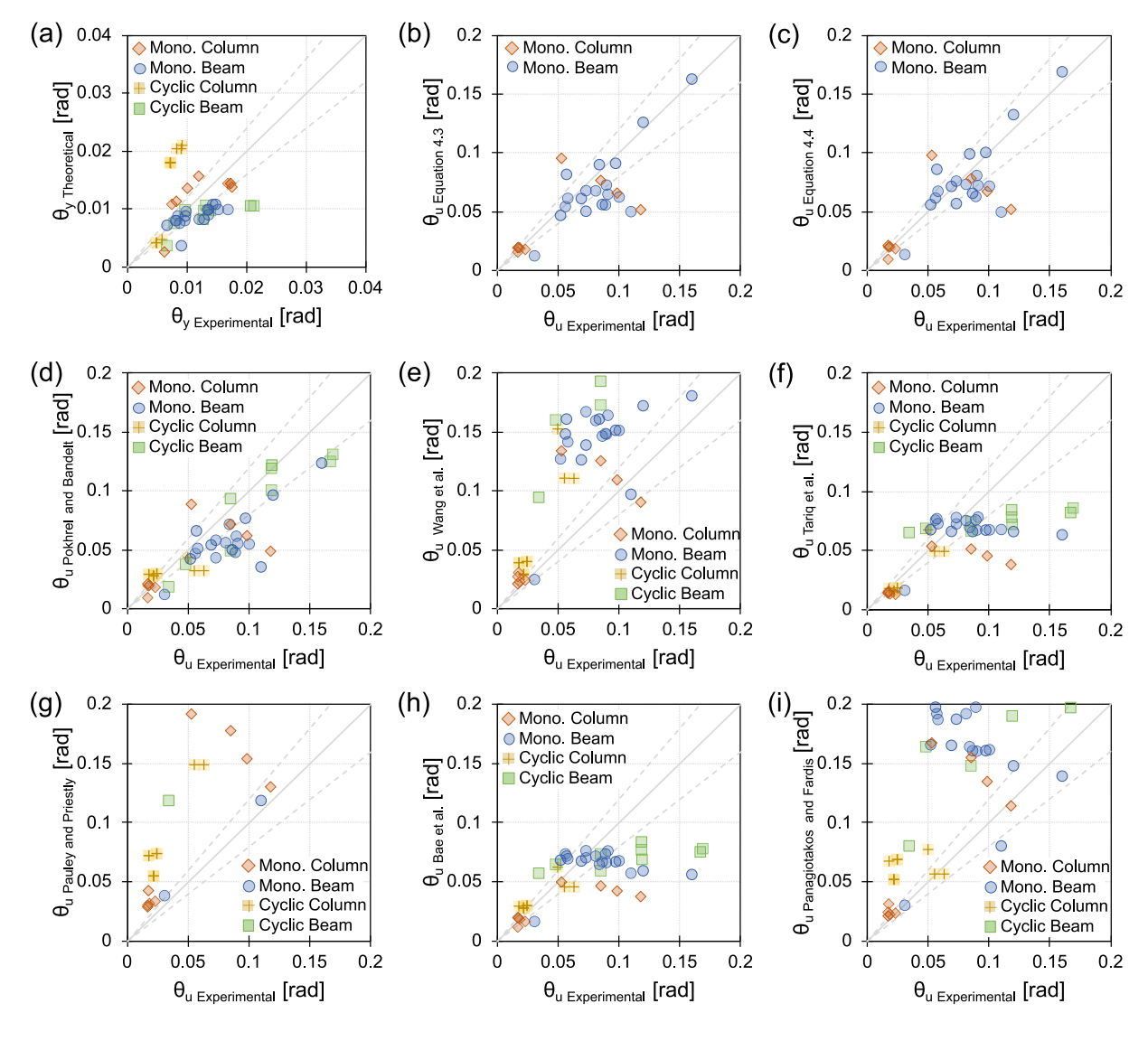


Fig. 8. Experimental versus analytically calculated yield and ultimate rotation capacities using various plastic hinge length expressions.

components was found to linearly increase with reinforcement ratio and shear span length and decrease with increasing HPFRCC tensile strength.

Following the characterization of the component's plastic hinge length across various design variables, two monotonic plastic hinge length expressions were proposed and verified against the rotation capacities of 28 experimental beams and columns. Both newly proposed expressions were shown to predict the experimental rotation capacities within 5%-9% on average depending on the expression, marking an overall improvement over previous expressions with average prediction accuracies within a range of 18.5%-153%. Despite the dependency of a component's plastic hinge length on its failure mechanism and axial load, the results of Sections 5 and 6 indicate that plastic hinge length expressions do not have to explicitly account for axial load. Rather, the effects of axial load on a component's rotational capacity can largely be accounted for in the calculation of its' section curvature. Lastly, the prediction ability of previously proposed cyclic plastic hinge length expressions was evaluated against 19 experimental responses. Cyclic plastic hinge length expressions, in particular, those by Polkhrel and Bandelt [18] and Tariq et al. [13], were found to predict the cyclic rotation of HPFRCC components within reasonable levels of accuracy (i.e., within 14.5% on average) over other expressions.

Based on the results of this study, the proposed plastic hinge length expressions coupled with appropriate hysteretic parameters can be used in both distributed and concentrated plasticity frameworks commonly employed by engineers and researchers, in order to evaluate the system-level performance of HPFRCC structures.

#### CRediT authorship contribution statement

**Joseph A. Almeida:** Writing – original draft, Visualization, Methodology, Investigation, Formal analysis. **Matthew J. Bandelt:** Writing – review & editing, Supervision, Resources, Project administration, Funding acquisition, Conceptualization.

# Declaration of competing interest

The authors declare that they have no known competing financial interests or personal relationships that could have appeared to influence the work reported in this paper.

#### Data availability

Data associated with this publication is publicly available on the National Science Foundation NHERI Data Depot [55].

#### Acknowledgments

This material is based upon work supported by the National Science Foundation, United States under Grant No. 2141955. Any opinions, findings, conclusions, or recommendations expressed in this material are those of the author(s) and do not necessarily reflect the views of the National Science Foundation.

#### References

- Council AT. Guidelines for performance-based seismic design of buildings. Tech. Rep. FEMA P-58-6, Applied Technology Council; 2018.
- [2] Naaman AE, Reinhardt HW. Proposed classification of HPFRC composites based on their tensile response. Mater Struct 2007;39(5):547–55. http://dx.doi.org/10. 1617/s11527-006-9103-2.
- [3] Wille K, Naaman AE, Parra-Montesinos GJ. Ultra-high performance concrete with compressive strength exceeding 150 MPa (22 ksi): A simpler way. Mater J 2011;108(1):46–54. http://dx.doi.org/10.14359/51664215.
- [4] Li VC. From micromechanics to structural engineering the design of cementitous composites for civil engineering applications. JSCE J Struct Mech Earthq Eng 1993;10(2):37–8, Accepted: 2011-06-16T18:11:36Z.
- [5] Wille K, El-Tawil S, Naaman A. Properties of strain hardening ultra high performance fiber reinforced concrete (UHP-FRC) under direct tensile loading. Cem Concr Compos 2014;48:53–66. http://dx.doi.org/10.1016/j.cemconcomp. 2013 12 015
- [6] Frank TE, Lepech MD, Billington SL. Experimental testing of reinforced concrete and reinforced ECC flexural members subjected to various cyclic deformation histories. Mater Struct 2017;50(5):232. http://dx.doi.org/10.1617/s11527-017-1102-y.
- [7] Wu C, Pan Z, Su RKL, Leung CKY, Meng S. Seismic behavior of steel reinforced ECC columns under constant axial loading and reversed cyclic lateral loading. Mater Struct 2017;50(1):78. http://dx.doi.org/10.1617/s11527-016-0947-9.
- [8] Chao S-H, Shamshiri M, Liu X, Palacios G, Schultz AE, Nojavan A. Seismically robust ultra-high-performance fiber- reinforced concrete columns. Struct J 2021;118(2):17–32. http://dx.doi.org/10.14359/51730391.
- [9] Aboukifa M, Moustafa MA. Experimental seismic behavior of ultra-high performance concrete columns with high strength steel reinforcement. Eng Struct 2021;232:111885. http://dx.doi.org/10.1016/j.engstruct.2021.111885.
- [10] Aboukifa M, Moustafa MA, Itani A. Comparative structural response of UHPC and normal strength concrete columns under combined axial and lateral cyclic loading. Spec Publ 2020;341:71–96. http://dx.doi.org/10.14359/51727025.
- [11] Gencturk B, Elnashai AS. Numerical modeling and analysis of ECC structures. Mater Struct 2013;46(4):663–82. http://dx.doi.org/10.1617/s11527-012-9924-0.
- [12] Tariq H, Jampole EA, Bandelt MJ. Fiber-hinge modeling of engineered cementitious composite flexural members under large deformations. Eng Struct 2019;182:62–78. http://dx.doi.org/10.1016/j.engstruct.2018.11.076.
- [13] Tariq H, Jampole EA, Bandelt MJ. Development and application of spring hinge models to simulate reinforced ductile concrete structural components under cyclic loading. J Struct Eng 2021;147(2):04020322. http://dx.doi.org/10.1061/ (ASCE)ST.1943-541X.0002891.
- [14] Tariq H, Jampole EA, Bandelt MJ. Seismic collapse assessment of archetype frames with ductile concrete beam hinges. Resilient Cities Struct 2023;2(1):103–19. http://dx.doi.org/10.1016/j.rcns.2023.02.008, Resilience of Structures to Earthquakes. URL https://www.sciencedirect.com/science/article/pii/S2772741623000091.
- [15] Gencturk B. Life-cycle cost assessment of RC and ECC frames using structural optimization. Earthq Eng Struct Dyn 2013;42(1):61–79. http://dx.doi.org/10. 1002/eqe.2193.
- [16] Bandelt MJ, Billington SL. Impact of reinforcement ratio and loading type on the deformation capacity of high-performance fiber-reinforced cementitious composites reinforced with mild steel. J Struct Eng 2016;142(10):04016084. http://dx.doi.org/10.1061/(ASCE)ST.1943-541X.0001562, Publisher: American Society of Civil Engineers.
- [17] Shao Y, Billington SL. Impact of UHPC tensile behavior on steel reinforced UHPC flexural behavior. J Struct Eng 2022;148(1):04021244. http://dx.doi.org/ 10.1061/(ASCE)ST.1943-541X.0003225.
- [18] Pokhrel M, Bandelt MJ. Plastic hinge behavior and rotation capacity in reinforced ductile concrete flexural members. Eng Struct 2019;200:109699. http://dx.doi. org/10.1016/j.engstruct.2019.109699.
- [19] Panagiotakos TB, Fardis MN. Deformations of reinforced concrete members at yielding and ultimate. Struct J 2001;98(2):135–48. http://dx.doi.org/10.14359/ 10181.
- [20] Haselton CB, Liel AB, Taylor-Lange SC, Deierlein GG. Calibration of model to simulate response of reinforced concrete beam-columns to collapse. ACI Struct J 2016;113(6). http://dx.doi.org/10.14359/51689245.
- [21] Haselton CB, Liel AB, Deierlein GG, Dean BS, Chou JH. Seismic collapse safety of reinforced concrete buildings. I: Assessment of ductile moment frames. J Struct Eng 2011;137(4):481–91. http://dx.doi.org/10.1061/(ASCE)ST.1943-541X.0000318, Publisher: American Society of Civil Engineers.

- [22] Pauley T, Priestley M. Principles of member design. In: Seismic design of reinforced concrete and masonry buildings. John Wiley & Sons, Ltd; 1992, p. 95–157. http://dx.doi.org/10.1002/9780470172841.ch3, Ch. 3.
- [23] Bae S, Bayrak O. Plastic hinge length of reinforced concrete columns. Struct J 2008;105(3):290–300. http://dx.doi.org/10.14359/19788.
- [24] Wang Z, Wang J, Tang Y, Gao Y, Zhang J. Lateral behavior of precast segmental UHPC bridge columns based on the equivalent plastic-hinge model. J Bridge Eng 2019;24(3):04018124. http://dx.doi.org/10.1061/(ASCE)BE.1943-5592.0001332, Publisher: American Society of Civil Engineers.
- [25] Mostafaei H, Kabeyasawa T. Axial-shear-flexure interaction approach for reinforced concrete columns. Struct J 2007;104(2):218–26. http://dx.doi.org/10. 14359/18534.
- [26] Goczek J, Supel L. Resistance of steel cross-sections subjected to bending, shear and axial forces. Eng Struct 2014;70:271–7. http://dx.doi.org/10.1016/ j.engstruct.2014.02.016.
- [27] Gusella F, Orlando M, Peterman KD. The impact of variability and combined loads on fuses in braced frames. Structures 2022;35:650–66. http://dx.doi.org/ 10.1016/j.istruc.2021.11.027.
- [28] Park R, Priestley MJN, Gill WD. Ductility of square-confined concrete columns. J Struct Div 1982;108(4):929–50. http://dx.doi.org/10.1061/JSDEAG.0005933.
- [29] Mendis P. Plastic hinge lengths of normal and high-strength concrete in flexure. Adv Struct Eng 2002;4(4):189–95. http://dx.doi.org/10.1260/ 136943301320896651.
- [30] Bandelt MJ, Billington SL. Bond behavior of steel reinforcement in high-performance fiber-reinforced cementitious composite flexural members. Mater Struct 2016;49(1–2):71–86. http://dx.doi.org/10.1617/s11527-014-0475-4.
- [31] Bandelt MJ, Billington SL. Simulation of deformation capacity in reinforced high-performance fiber-reinforced cementitious composite flexural members. J Struct Eng 2018;144(10):04018188. http://dx.doi.org/10.1061/(ASCE)ST.1943-541X.0002174.
- [32] Shao Y, Hung C-C, Billington SL. Gradual crushing of steel reinforced HPFRCC beams: Experiments and simulations. J Struct Eng 2021;147(8):04021114. http://dx.doi.org/10.1061/(ASCE)ST.1943-541X.0003080.
- [33] Shao Y, Ostertag CP. Bond-slip behavior of steel reinforced UHPC under flexure: Experiment and prediction. Cem Concr Compos 2022;133:104724. http://dx.doi. org/10.1016/j.cemconcomp.2022.104724.
- [34] DIANA finite element analysis documentation, release 10.5. 2021, URL https://manuals.dianafea.com/d105/Diana.html.
- [35] Fischer G, Li VC. Effect of matrix ductility on deformation behavior of steelreinforced ECC flexural members under reversed cyclic loading conditions. Struct J 2002;99(6):781–90. http://dx.doi.org/10.14359/12343.
- [36] Marchand P, Baby F, Khadour A, Rivillon P, Renaud J-C, Baron L, Généreux G, Deveaud J-P, Simon A, Toutlemonde F. Response of UH-PFRC columns submitted to combined axial and alternate flexural loads. J Struct Eng 2019;145(1):04018225. http://dx.doi.org/10.1061/(ASCE)ST.1943-541X.0002209, Publisher: American Society of Civil Engineers.
- [37] Hung C-C, Hu F-Y, Yen C-H. Behavior of slender UHPC columns under eccentric loading. Eng Struct 2018;174:701–11. http://dx.doi.org/10.1016/j.engstruct. 2018.07.088.
- [38] ACI code 318-19: Building code requirements for structural concrete and commentary. 2019, http://dx.doi.org/10.14359/51716937.
- [39] Li VC, Wang S, Wu C. Tensile strain-hardening behavior of polyvinyl alcohol engineered cementitious composite (PVA-ECC). Mater J 2001;98(6):483–92. http://dx.doi.org/10.14359/10851.
- [40] Blunt JD, Ostertag CP. Deflection hardening and workability of hybrid fiber composites. Mater J 2009;106(3):265–72. http://dx.doi.org/10.14359/56551.
- [41] Kesner K, Billington S. Investigation of infill panels made from engineered cementitious composites for seismic strengthening and retrofit. J Struct Eng 2005;131(11):1712–20. http://dx.doi.org/10.1061/(ASCE)0733-9445(2005)131: 11(1712).
- [42] Trono W, Jen G, Panagiotou M, Schoettler M, Ostertag CP. Seismic response of a damage-resistant recentering posttensioned-HYFRC bridge column. J Bridge Eng 2015;20(7):04014096. http://dx.doi.org/10.1061/(ASCE)BE.1943-5592.0000692, Publisher: American Society of Civil Engineers.
- [43] Li VC. Engineered cementitious composites (ECC) material, structural, and durability performance. In: Concrete construction engineering handbook. CRC Press; 2008, Accepted: 2011-06-16T18:09:49Z.
- [44] Graybeal BA. Material property characterization of ultra-high performance concrete. Report FHWA-HRT-06-103, Federal Highway Administration; 2006.
- [45] Yoo D-Y, Yoon Y-S. Structural performance of ultra-high-performance concrete beams with different steel fibers. Eng Struct 2015;102:409–23. http://dx.doi.org/ 10.1016/j.engstruct.2015.08.029.
- [46] Chi Y, Xu L, Zhang Y. Experimental study on hybrid fiber-reinforced concrete subjected to uniaxial compression. J Mater Civ Eng 2014;26(2):211–8. http: //dx.doi.org/10.1061/(ASCE)MT.1943-5533.0000764.
- [47] Moreno-Luna D. Tension stiffening in reinforced high performance fiber reinforced cement based composites (Ph.D. thesis), Stanford University; 2014, p. 270, Copyright Database copyright ProQuest LLC; ProQuest does not claim copyright in the individual underlying works; Last updated 2023-06-21.

- [48] Moreno DM, Trono W, Jen G, Ostertag C, Billington SL. Tension stiffening in reinforced high performance fiber reinforced cement-based composites. Cem Concr Compos 2014;50:36–46. http://dx.doi.org/10.1016/j.cemconcomp.2014. 03.004.
- [49] Naeimi N, Moustafa MA. Compressive behavior and stress-strain relationships of confined and unconfined UHPC. Constr Build Mater 2021;272:121844. http://dx.doi.org/10.1016/j.conbuildmat.2020.121844.
- [50] Pokhrel M, Bandelt MJ. Material properties and structural characteristics influencing deformation capacity and plasticity in reinforced ductile cement-based composite structural components. Compos Struct 2019;224:111013. http://dx.doi.org/10.1016/j.compstruct.2019.111013.
- [51] Bandelt MJ, Frank TE, Lepech MD, Billington SL. Bond behavior and interface modeling of reinforced high-performance fiber-reinforced cementitious composites. Cem Concr Compos 2017;83:188–201. http://dx.doi.org/10.1016/j.cemconcomp.2017.07.017.
- [52] Li L-Z, Bai Y, Yu K-Q, Yu J-T, Lu Z-D. Reinforced high-strength engineered cementitious composite (ECC) columns under eccentric compression: Experiment and theoretical model. Eng Struct 2019;198:109541. http://dx.doi.org/10.1016/ j.engstruct.2019.109541.
- [53] McKenna F, Scott MH, Fenves GL. Nonlinear finite-element analysis software architecture using object composition. J Comput Civ Eng 2010;24(1):95–107. http://dx.doi.org/10.1061/(ASCE)CP.1943-5487.0000002, Publisher: American Society of Civil Engineers.
- [54] Shao Y, Billington SL. Flexural performance of steel-reinforced engineered cementitious composites with different reinforcing ratios and steel types. Constr Build Mater 2020;231:117159. http://dx.doi.org/10.1016/j.conbuildmat.2019.117159.
- [55] Almeida J, Bandelt M. High fidelity numerical modeling of hpfrcc beams and columns. Designsafe-CI 2024. http://dx.doi.org/10.17603/DS2-S1WR-B775.